Supplementary Information for

Dynamics of hydraulic and contractile wave-mediated fluid transport during *Drosophila* oogenesis

Authors

Jasmin Imran Alsous, Nicolas Romeo, Jonathan A. Jackson, Frank Mason, Jörn Dunkel, Adam C. Martin

Corresponding authors

Adam C. Martin (acmartin@mit.edu)

Jörn Dunkel (dunkel@mit.edu)

This PDF file includes:

Other supplementary materials for this manuscript include the following:

Image and Data Analysis Methods

Image Analysis. We used FIJI (1) and Bitplane's Imaris (2) to analyze our images and movies, and Matlab (3) for aligning data and generating plots. Measurements and sample sizes are recorded in Table S2.

Measurements of cell sizes, volume estimates, and creation of cell volume time courses. Nurse cells are large cells (~50-70 µm in diameter at onset of NC dumping) and often move noticeably in all three dimensions during NC dumping. As a result, we were unable to consistently capture the entire NC cluster during live imaging, preventing us from obtaining complete cell volume measurements. Instead, we used area measurements as a proxy for volume measurements, assuming cells are roughly spherical and that the volume of a cell could be calculated from its midplane area as $V = \frac{4}{3\sqrt{\pi}} A^{3/2}$. After normalizing to initial sizes, this allowed estimation of normalized volumes as $V/V_0 = (A/A_0)^{3/2}$, where A_0 and V_0 are the area and estimated volume at the beginning of dumping for that cell. Areas were measured in FIJI by manually outlining each cell in the z-plane of largest cross-section at roughly 5-minute time intervals over the usable course of the movie. We confirmed that area measurements are a good proxy for cell volume by comparing the result of raising our normalized area measurements to the 3/2 power with the few usable normalized volume measurements acquired using Imaris (Fig. S1, B to D). Nurse cells were not included in the analysis if any of the following occurred before enough data could be taken to generate a trajectory for changes in cell volume during NC dumping: the cell was positioned in z such that its cross-sectional area did not show a maximum within the imaged depth, the cell fused with a neighbor early in the acquired time course, or the cell shape was significantly deformed from a sphere when viewed in 3D. Times taken from microscopy metadata were shifted either to align all traces by the time of their dumping onset or to align by wave/deformation onset; that is, to make $t = 0$ correspond to the first frame at which the behavior in question was observed. Because the time required to complete a z-stack varied between movies, calculation of mean time courses of normalized volume estimates required temporal alignment. Volume time courses were aligned in Matlab through linear interpolation to one-minute time intervals. For calculations of layer averages, individual time courses were then truncated to times at which data was collected for all cells to prevent discontinuities in the mean time course resulting from a variable number of measurements. For mean time courses of all cells together, a larger time range was included, and means were produced by grouping data into 20-minute bins and plotting bin averages. Time courses of NC cluster and oocyte lengths (Fig. S1A) were generated using the same methods as for layer averages but using normalized length measurements of the NC cluster and oocyte along the long axis of the egg chamber instead of areas. For the

NC cluster and oocyte length time courses, $N = 4$ egg chambers for $t = $ -28 to 130 minutes and $N = 3$ egg chambers at other times.

Nucleus size ratio measurements. To measure the ratio of nuclear to cell radius at dumping onset, polygon regions of interest (ROIs) were first drawn over a nucleus and the cell containing it at $t = 0$. Areas of the two ROIs (A_n, A_c) were measured in FIJI, and the ratio of effective radii, β, was defined as $\beta = r_n/r_c = \sqrt{A_n/A_c}$. As with the cell size measurements described above, the area used for the nucleus was that of its midplane slice. We found a ratio of 55±5% (standard deviation, $N = 27$ nurse cells from 6 egg chambers).

Dumping onset kymographs and plots. Using maximum intensity projections (MIPs) through z, a linear ROI was drawn across the long axis of egg chambers from posterior to anterior (see dashed line in Fig. 2A) using FIJI, and the MultipleKymograph plugin was used to generate kymographs of myosin (*sqh::GFP* or *sqh::mCh*) or membrane (*Ecad::GFP* or *gap43::mCh*) intensity over time along the line. To generate a plot of average dumping onset rate and progression, several such kymographs were generated, the front between centripetal follicle cells and the NC cluster (i.e. the posterior boundary of the NC cluster) was outlined manually on the kymograph, and its coordinates were taken from FIJI. Coordinates of the fronts were input to Matlab and aligned by subtracting the baseline (initial position of the front). Linear measurements of the posterior NC cluster boundary location showed an S-shaped curve with a clear inflection point, so interpolation was performed as described above and times were shifted to align the inflection in each time course in order to avoid ambiguities in determining dumping onset by eye.

Time measurements of wave onset. Dumping and wave onset times were collected by viewing movies in FIJI. Time differences between dumping and wave onset were determined, cells were grouped by layer, and layer statistics were calculated using Microsoft Excel.

Analysis of actomyosin levels. Mean and standard deviation of fluorescence intensity along a segment of the cell perimeter were measured for different time points for germline cysts labeled with either *sqh::mCh* or *sqh::GFP*. Segments were chosen to avoid tricellular junctions, where Sqh intensity was typically much higher than surrounding regions. In addition, the top and bottom 2-3 slices were excluded from the analysis and the outer curves of the nurse cells were avoided to prevent myosin variation in the surrounding follicle cells from affecting the measurements. Note that the ellipsoidal shape of the germline cysts resulted in changes in intensity solely from the amount of tissue between the objective and the optical section; unlike for a flat tissue, this intensity decrease was not consistent across a plane. As a result, segments of the cell perimeter were limited in length and confined to regions without a noticeable intensity gradient along the

ROI. Lastly, since a measurement of intensity alone would not differentiate between actual relative biological changes in myosin levels/distribution and imaging artifacts, the coefficient of variation (COV), defined as the ratio of standard deviation to mean (σ/μ), was calculated for each measurement to determine the fractional variability in intensity along the membrane and allow comparison between different cells and germline cysts (Fig. 1E; Fig. S3B). As a control, the same process was repeated for cells labeled with *Resille::GFP*, a membrane marker (Fig. S3C). Measurements were grouped into three phases, the first corresponding to times prior to wave onset, the second to times at which the membrane showed only uniform shrinkage while maintaining cell shape, and the third to times at which the membrane deformed heavily and non-uniformly, changing cell shape. Average values of the COV for each group were calculated by weighting each measured COV by the length of the corresponding ROI. Two-tailed Welch's *t* tests were performed using Matlab's ttest2 function with the 'unequal variance' option.

Generation of actomyosin kymographs. For wild-type (WT) wave behavior kymographs, ROIs were drawn on MIP time-lapse images along a curved path following the wave fronts (colliding waves), along the cell perimeter (rotating waves), or across the cell diameter (traveling rings), and wave kymographs showing Sqh levels were generated using FIJI as described above. MIPs through *z* were created using built-in FIJI tools. Cells used for actin behavior kymographs and the RhoGAP15B RNAi myosin kymograph moved significantly over the time period of interest, so ROIs were drawn around the perimeter of MIP time-lapse images, starting at the same location of the cell in each frame. Intensities around these perimeters were measured in FIJI, input to Matlab, aligned and scaled to their fractional position along the cell perimeter, and displayed as kymographs. The RhoGAP15B RNAi kymograph in Fig. 3K is of a layer 4 cell sufficiently long after dumping onset that a WT cell would have begun non-uniform contractions.

Quantification of cell deformation. Cell outlines were manually drawn in FIJI over MIPs of a cytoplasmic marker (*Clip170::GFP*) or a membrane marker (*Resille::GFP*); their coordinates were taken and input to Matlab, where the cell centroid and projected area were calculated and used to create a circular outline with the same centroid and area as the cell. At each time point, deviations of the measured outline from the circle were then calculated at 180 evenly-spaced angles from the centroid and normalized by the effective cell radius $r_{eff,t} = \sqrt{A_t/\pi}$ (Fig. S2): for a given angle θ_n at which the projected cell outline is a distance $r_{n,t}$ from the centroid, we defined fractional deformation as $\alpha_{n,t} = \frac{r_{n,t}-r_{eff,t}}{r_{eff,t}}$. To account for non-circular shapes of cells, which could change over time solely due to volume decrease, the magnitude of change in deformation profile from one time point to the next was then calculated and the root-mean-square (rms) value taken:

$$(\Delta\alpha_{rms})_t = \sqrt{\frac{1}{N}\sum_{n=1}^{N}\left(\alpha_{n,t} - \alpha_{n,(t-1)}\right)^2} \qquad (1)$$

where n indexes the angle and t the time point; $N = 180$ here. Measurements were aligned in time as described above so time spacing between elements of α was the same for each cell.

Reflection-mode microscopy flow behaviors. For flow behavior quantification, types of flow were broken into two main categories: intercellular flow (through ring canals) and intracellular flow (induced within a cell by actomyosin waves). For intercellular flow, the direction could be further categorized as either anterior-to-posterior or posterior-to-anterior; the latter is the opposite of that required for complete NC dumping. For each movie of WT or RhoGAP15B-depleted germline cysts, the duration of each type of flow behavior was recorded. For WT, there were 6 events of intercellular flow spanning 30 minutes total; for RhoGAP15B knockdowns, there were 29 events spanning 54 minutes. There were 28 intracellular flow events in WT for a total of 239 minutes, and 82 intracellular events spanning 338 minutes in RhoGAP15B knockdowns. Fig. 4E represents the actual duration of intracellular events, while the fraction of time undergoing each intercellular behavior was calculated and used to generate Fig. 4F.

Ring canal growth kinetics measurements. Z-stacks of egg chambers dissected at various stages (2 through 11) were acquired as described above. Inner ring canal diameter was measured using Imaris or Zen for every fully visible, undeformed ring canal (26 egg chambers, 10-15 ring canals per chamber, 370 canals total). The stage of oogenesis was estimated using morphological and size features (4) and converted to developmental time (5). Errors in matching measurements of ring canal diameters to a developmental stage within oogenesis arise from inherent variability in developmental rates and uncertainties in determining the exact age of the egg chamber as staging is based on morphological and size features.

Theory

Model. We modeled hydrodynamic flow on the stereotypical 16-cell tree that is the *Drosophila*'s germline cyst. Cells i and j are connected by ring canals, each of which can be approximated as a small cylindrical pipe of radius r_{ij} and length L. The viscosity of cytoplasm in *Drosophila* has been estimated *in vivo* (6) as $\mu \simeq 1 Pa \cdot s$. At low Reynolds numbers

$$(Re = \frac{\rho_o U a}{\mu} \approx \frac{10^3 kg}{m^3} \times \frac{10^{-6} m}{s} \times \frac{10^{-6} m}{1 Pa \cdot s} = 10^{-9} \ll 10^{-3},$$

with U a characteristic speed, a a length scale and ρ_o the density of the cytoplasm), flow through the ring canals is assumed to be incompressible Poiseuille flow. In this case, flow J_{ij} from cell j to i is proportional to the difference in their respective pressures $(p_j - p_i)$, with the proportionality constant given by the hydraulic conductance G_{ij}.

The change in the volume of cell i is then determined by the total fluxes in and out of the cell:

$$\frac{dV_i}{dt} = \sum_{\langle i,j \rangle} J_{ij} = \sum_{\langle i,j \rangle} G_{ij}(p_j - p_i). \tag{2}$$

Here, the sum runs over the set of cells j connected to cell i by ring canals. Summing over all the cells, one can verify that the total cytoplasmic volume is conserved throughout the germline cyst, i.e. $\sum_i dV_i/dt = 0$ at all times.

Balloon pressure law. We model each cell i as a spherical 'balloon', with interior pressure p_i relative to the homogeneous pressure outside given by the modified Laplace pressure law (7):

$$p_i = \frac{2\gamma}{R_i}\left(1 - \left(\frac{R_{0,i}}{R_i}\right)^6\right). \tag{3}$$

Here, $R_i = (3V_i/4\pi)^{1/3}$ is the radius of the i-th balloon, and γ is the surface tension of the shell, understood here as the generic energy cost to build an interface. As long as the cell is roughly spheroidal, the spherical approximation will not qualitatively alter the results.

To gain intuition about the behavior of this pressure law, consider two balloons (or two cells) that are connected by an open canal. There are two possible equilibrium configurations for which the pressure in both balloons is equal. In the first case, both balloons are of equal size and the system does not deviate from its initial configuration. In the second case, the balloons assume unequal sizes; that is, an initial size imbalance will be amplified until the pressures balance out. For instance, if $R_p = 7^{1/6}R_0 \approx 1.38R_0$ is the radius at maximum pressure and assuming that initially both balloon radii are larger than R_p, the initially larger balloon will grow to a radius $R_{large} \gg R_p$, whereas the other will shrink down to a radius $R_{small} < R_p$. Note that as R_i grows relative to the zero-pressure radius $R_{0,i}$, one recovers the usual Laplace pressure law, $p_i = 2\gamma/R_i$.

Alternative pressure laws. While the microscopic nature of a nurse cell is much more complex than a rubber balloon, cells can be considered effectively viscoelastic, with a filamentous cytoskeleton bearing similarities to crosslinked semiflexible polymer networks such as rubber (8). Merritt and Weinhaus obtained the above pressure law for the case of an isothermal spherical rubber balloon, using a specific constitutive equation (also called *stress-strain equation*) (7), first derived by James and Guth for rubber in 1943 (9). In fact, as shown previously (10), one would obtain the same functional form for the pressure law for a neo-Hookean material, which itself is a particular case of a Mooney-Rivlin material for small enough extensions. Mooney-Rivlin materials are generally considered to be appropriate models of incompressible rubber-like materials and have been widely used to describe biological tissues, including the cellular cortex (11). If we were to relax the assumption of incompressibility, another family of constitutive relations would follow the Blatz-Ko model (10) and more complex variants. Since cells are usually considered more fluid-like than solid (12), the assumption of incompressibility is reasonable, rendering the Merritt and Weinhaus law an appropriate framework for this problem.

From a more physical viewpoint, to illustrate how a different microscopic model would provide a different power law correction to Young-Laplace's law, consider for instance a spherical shell of radius R consisting of particles that interact according to an repulsive short-range pair potential $V(x - y) = -g\delta^2(x - y)$. Assuming the particles' surface density is uniform $\rho(x) = \rho = N/(4\pi R^2)$, the energy contribution of this interaction is:

$$F = \frac{1}{2}\int d^2x\, d^2y\, \rho(x)\rho(y)V(x - y) = -\frac{g}{2}4\pi R^2\rho^2.$$

In the presence of a surface tension, the differential of free energy would be, at constant temperature,

$$dF = -pdV + \gamma dA$$

where dA is the variation in area. The pressure as a function of radius would then be given by

$$p = -\frac{\partial F}{\partial V} + \gamma \frac{dA}{dV} = \frac{2\gamma}{R} - \frac{gN^2}{8\pi^2}\frac{1}{R^5} = \frac{2\gamma}{R}\left(1 - \left(\frac{R_0}{R}\right)^4\right)$$

with $2\gamma R_0^4 = gN^2/8\pi^2$. Here we see that the repulsive interaction potential ends up contributing a $1/R^n$ – a correction to Laplace's law.

Lastly, to test out whether different 'elastic' $1/R^n$ terms provide qualitative agreement with the data, we ran different simulations with varying values of n. While the slopes of curves varied, the directionality and layer-wise hierarchy of dumping order was preserved (Fig. S4B).

Hydraulic conductance. Nurse cells in the germline cyst are connected by ring canals. Assuming Poiseuille-type flow (13), the hydraulic conductance G of a cylinder of radius r and length L is given by:

$$G = \frac{\pi r^4}{8\mu L} \tag{4}$$

We use this formula as an initial guess for the hydraulic conductance G_{ij} between cells i and j at the onset of NC dumping, adopting typical parameters $r \approx 5\mu m$ and $L \approx 2\mu m$ inferred from experimental imaging data. However, the Poiseuille approximation is only valid for $L \gg r$, and we expect the Poiseuille approximation to underestimate the actual conductance. We therefore scanned conductance values in the vicinity of the Poiseuille approximation, as described below.

To test whether such a surface tension-driven flow model could capture the observed dynamics of intercellular networked transport through ring canals, we first estimated the minimal effective surface tension required for Laplace pressure-driven flow at magnitudes comparable to those observed experimentally. The relative contributions of cortical tension versus in-plane membrane tension to cell surface tension are known to vary (14). Here, we combine both contributions into a single effective surface tension parameter γ that can be estimated from measurable quantities as described below:

$$\gamma = \frac{4\mu LRJ}{\pi r^4} \tag{5}$$

To estimate an upper bound on J, the magnitude of flux through a single ring canal, we used the steepest rate of change in cell volume (Fig. 2C), multiplied it by the average volume of a layer 1 cell at NC dumping onset and obtained $J = 40\mu m^3/s$.

Using $\mu \simeq 1 Pa \cdot s$, $L = 2\mu m$, $R \approx 30\mu m$, $J = 40\mu m^3/s$, $r = 5\mu m$, we find a value of approximately 4 pN/μm for γ. This estimate for γ is at the lower end of literature reported values (15), consistent with the known fact that the nurse cell cluster has a relatively low basement membrane stiffness (16). We therefore contend that surface tension is sufficient for driving the observed transport dynamics.

In our subsequent calculations, we assumed that cell surface tension is constant in time for all cells as transport unfolds, which is supported by previous studies showing that plasma membrane tension is actively buffered (e.g. through endocytosis) (17,18). We also assume that cell surface tension is equal for all cells, justified by the fact that the cortical cytoskeletal network is invariant across cells within the germline cluster, and that it does not appear to be significantly altered during the first phase of NC dumping, i.e., during the phase of surface tension-driven flow.

Additionally, to account for cell-to-cell variability in effective cell surface tension, we explored the effects of fluctuations of surface tension between cells in the model. To this end, we first adjusted the model to the experimental data, and subsequently allowed for approximately 10% surface tension fluctuations to account for variations in shape, basement membrane stiffness and other factors of cell-to-cell variability (also see the 'Simulations and optimization' section below).

Dimensionless equations. Writing out equation (2) fully yields:

$$\frac{dV_i}{dt} = \sum_{\langle i,j\rangle} \frac{\pi\gamma r_{ij}^4}{4\mu L}\left[\frac{1}{R_j}\left(1 - \left(\frac{R_{0,j}}{R_j}\right)^6\right) - \frac{1}{R_i}\left(1 - \left(\frac{R_{0,i}}{R_i}\right)^6\right)\right] \tag{6}$$

To rewrite this equation in nondimensionalized form we define the characteristic time scale $\tau_0 = 4\mu L/(\pi\gamma)$ and length scale ℓ_0 such that the initial oocyte volume is $100\ell_0^3 = 10^6 \mu m^3$, yielding $\ell_0 \approx 20\mu m$. Using our estimate for γ from above, we find $\tau_0 \approx 0.6$ s. Defining the dimensionless radius $\hat{R}_i = R_i/\ell_0$, time $\hat{t} = t/\tau_0$, and volume $\hat{V}_i = V_i/\ell_0^3$, the dynamical equation takes the dimensionless form

$$\frac{d\hat{V}_i}{d\hat{t}} = \sum_{\langle i,j\rangle} \hat{G}_{ij}\left[\frac{1}{\hat{R}_j}\left(1 - \left(\frac{\hat{R}_{0,j}}{\hat{R}_j}\right)^6\right) - \frac{1}{\hat{R}_i}\left(1 - \left(\frac{\hat{R}_{0,i}}{\hat{R}_i}\right)^6\right)\right] \tag{7}$$

where the dimensionless pressure is given by

$$\hat{p}_i = \frac{1}{\hat{R}_i}\left(1 - \left(\frac{\hat{R}_{0,i}}{\hat{R}_i}\right)^6\right).$$

To generalize the model beyond the Poiseuille approximation, we introduced in equation (7) the *dimensionless conductances* $\hat{G}_{ij} = (r_{ij}/\ell_0)^4$. Written in terms of $\hat{G}_{ij}$, the model does not depend on the precise scaling of G_{ij} with r_{ij}, and adjusting $\hat{G}_{ij}$ to achieve the best-fit of the model solution to the experimental data provides a way of measuring the hydraulic conductances.

Initial conditions and parameters. At $t = 0$, the sixteen cells have a well-characterized cell size pattern, as nurse cells further from the oocyte are smaller than those that are closer. The initial size distribution is determined as follows (19):

1) the oocyte has a volume V_0 equal to the sum of all the nurse cells' volumes combined
2) nurse cells at the same distance $d = 1, 2, 3, 4$ from the oocyte have the same cell volume V_d set by

$$\frac{V_{d+1}}{V_0} = \left(\frac{V_d}{V_0}\right)^{\nu} \text{ with } \nu \approx 0.84.$$

Using these initial conditions, we computed the time-evolution of each cell's volume by numerically integrating the above set of ordinary differential equations. Our simulations (described in the following section) showed that the form of the trajectories depends strongly on the following parameters:

(i) Dimensionless conductances $\hat{G}_d$: To compensate for the inaccuracy of the Poiseuille formula, we adjusted the dimensionless conductance to obtain agreement with our experimental observations. Assuming that all ring canals at edge distance d from the oocyte have the same size r_d (Fig. S5A), all ring canals at edge distance d also have the same dimensionless conductance $\hat{G}_d$. We then allow for variations of $\hat{G}_d$ by allowing the effective ring canals radii $r_d := \ell_0 \hat{G}_d^{1/4}$ to vary from their corresponding average experimental values by up to plus or minus 60% as described in the section 'Fitting procedure' below. As expected, the best-fit effective ring canal radii are larger than the directly measured ring canal radii, confirming that the Poiseuille formula Eq. (4) underestimates the actual hydraulic conductance. Test simulations with equal ring canal sizes do not reproduce the experimentally observed dumping hierarchy.

(ii) Zero-pressure radius: We assumed all cells have a zero-pressure radius $R_{0,i} = \rho R_i(t = 0)$, where ρ is an adjustable parameter between 0 and 1.

Overall, this yields a total of five tunable parameters: the four hydraulic conductances $\hat{G}_d$ and the zero-pressure radius scale parameter ρ. A summary of the initial conditions and adjustable parameters is given in Table S3.

Simulations and Optimization

Implementation. The simulations were implemented in Python 3 augmented with the NumPy/SciPy libraries. The regular scipy.integrate.solve_ivp routine was used to solve the system of ordinary differential equations. Simulations were run until the system reached steady state. We have not conducted a full analysis of the stability of the fixed points in a more general setting. However, since our initial conditions are hierarchical, with the oocyte significantly larger than the next largest NCs, the dynamics most likely lie in the basin of attraction of the "1 large; 15 small" solution. Furthermore, those dynamics do not lead to perfectly empty balloons at steady state; indeed, as our experimental data show, completion of the dumping process requires active contractions, which are not included in the network flow model; we can therefore only reliably compare our simulation results with experimental data before the effects of myosin activity become too important, and the simulated steady-state has no physical relevance.

Fitting procedure. Experimental measurements provided us with the relative cross-sectional areas of cells, which we averaged per layer of cells at distance d from the oocyte. We then estimated the relative experimental volumes

$$V_d^{exp}(t)/V_d^{exp}(t=0) = \left(A_d^{exp}(t)/A_d^{exp}(t=0)\right)^{\frac{3}{2}},$$

with time t expressed in units of τ_0. Our simulations then yield a set of volume trajectories $V_d^{sim}(t)$ for the average volume of cells in layer d.

Since the model developed here describes the first phase of NC dumping, namely, surface tension-driven flow, and does not include the effect of the actomyosin contractility, we compared our trajectories to experimental data taken before onset of actomyosin contractility only. Experiments show that this occurs when cells reach a characteristic fraction of their initial volume $V_{wave} \approx 0.25V(t=0)$ (Fig. S3). The sum of squares error between the experimental and simulation datapoints was then computed for each of the layer-averaged cross-sectional areas of cells, with a set of weights $g_d = (4/15, 6/15, 4/15, 1/15)$ such that $\sum_d g_d = 1$, reflecting the number of nurse cells in each layer. The error is then given by:

$$E = \sum_i \sum_{layers\ d=1}^{4} g_d\left(V_d^{exp} - V_d^{sim}\right)^2(t_i) \tag{8}$$

This procedure was repeated as we searched through a grid of possible parameter values around their experimental averages, yielding the error plots shown in Fig. S4A (the final grid search was over 3.2 million simulations). The scanned parameter ranges and the best fit parameters that resulted in the smallest error E are summarized in Table S3.

Cell-to-cell variability. Once the parameters were determined through the method described above, we introduced fluctuations between individual cells in the effective surface tension. To that end, we sampled surface tension for each cell as $\gamma_i = \gamma_c(1 + \sigma \chi_i)$, where χ_i is a random variable sampled from the standard normal distribution with $\sigma = 0.1$. Results averaged over $N = 5{,}000$ trials are presented (Fig. S4C), where the envelope reflects one standard deviation of the fluctuation.

Ring canal fits. Measured ring canal diameters (Fig. S5A) were averaged for each layer and each stage. Exponential functions of the form $r(t) = r_o e^{t/\tau}$ were then fit to the averages using the 'fit' function in Matlab. The fit parameters are as follows: $r_o = 0.82, 0.55, 0.44,$ and 0.67 µm and $\tau = 34.8, 31.2, 29.1,$ and 38.0 hours for L1-L4, respectively. Values of R^2 are $0.93, 0.88, 0.85,$ and 0.83, respectively.
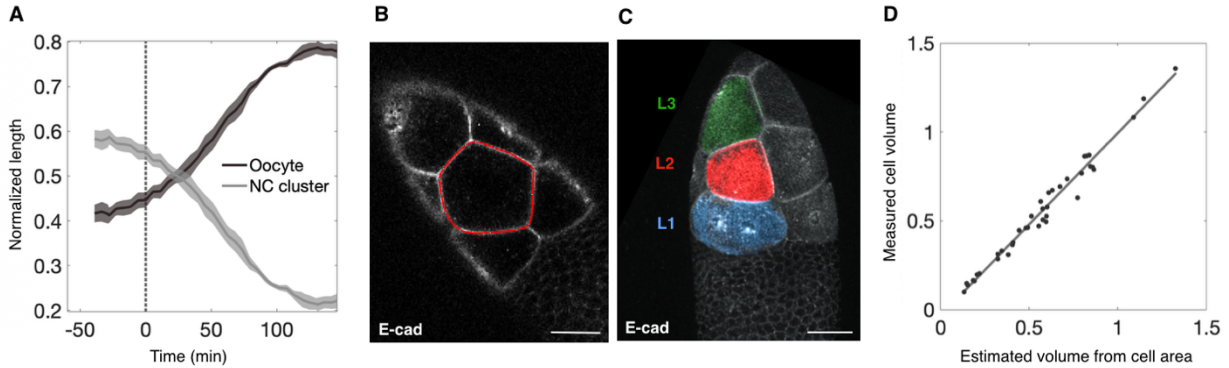
Figures S1 to S8

Fig. S1. Verification of cell volume measurements. A. Plot of fractional lengths of the NC cluster and oocyte during NC dumping ($N = 4$ egg chambers). Line at $t = 0$ indicates onset of NC dumping. **B**. Optical section of an egg chamber expressing *Ecad::GFP*, used to measure NC area as indicated by red outline. **C**. 3D-rendered confocal image of an egg chamber expressing *Ecad::GFP* with surface reconstructions of NCs for measuring NC volume. Scale bar in **B** and **C** = 40 μm. **D**. Plot of normalized NC volume (V/V_o) as measured from 3D Imaris surface reconstructions versus normalized NC volume estimated from cell area measurements in FIJI, showing good agreement between both measurements; solid line shows the best fit line; $R^2 = 0.98$, with slope = 1.03.
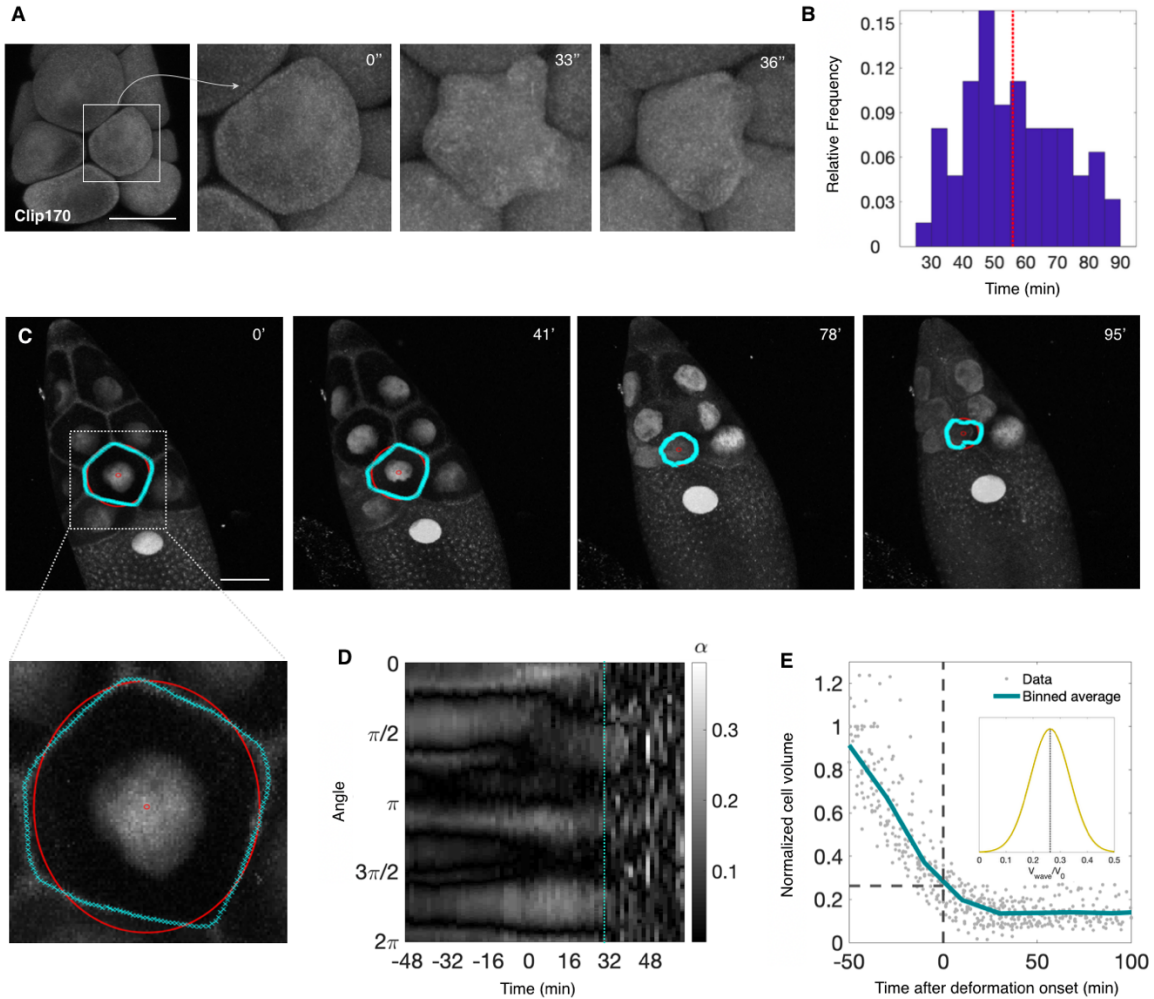
Fig. S2. Quantification of nurse cell shape deformations. A. 3D-rendered time-lapse confocal images of an egg chamber expressing *Clip170::GFP*; blowups show a cell contracting and deforming nonuniformly with onset of actomyosin waves. **B**. Histogram of time (min) following onset of NC dumping at which nonuniform NC deformations are first observed (red line shows average, $N = 63$ cells). **C**. Time-lapse maximum intensity projections (MIPs) of an egg chamber with labeled membranes (*Resille, Res*) and nuclei (*Proliferating Cell Nuclear Antigen, PCNA*); outlined NC is analyzed in **D**. Blowup shows features used to quantify cell shape deformation: red dot indicates the cell's centroid; red outline indicates a circle with the same projected area as the NC; cyan outline shows point-wise cell shape. Scale bar in **A** and **C** = 40 μm. **D**. Kymograph of fractional deviation of NC shape from a circle, α, based on Resille, obtained from the MIP in **C**; line (cyan) marks beginning of nonuniform cell deformations. **E**. NC volume changes of different NCs ($N = 30$ cells) during NC dumping; $t = 0$ defines onset of nonuniform cell deformations. Inset shows the distribution of normalized cell volumes (V/V_o) at onset of cell deformations.

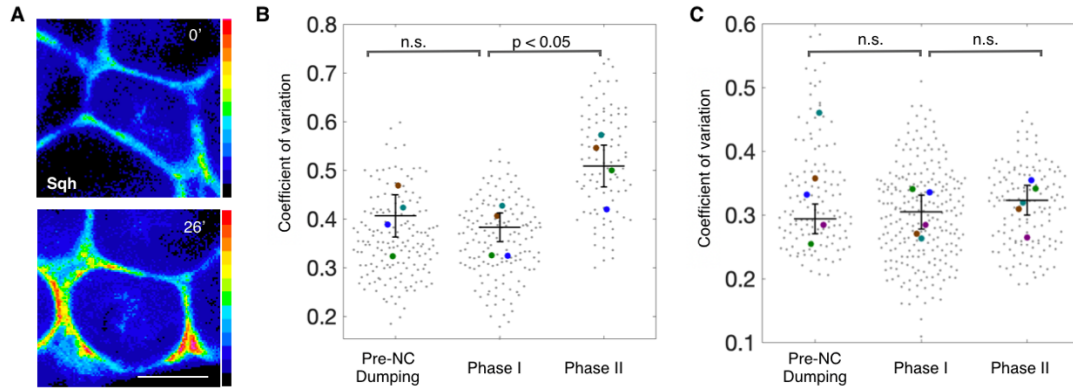**Fig. S3. Verification of Sqh distribution measurements. A**. Heat map of Sqh intensity along the perimeter of an NC in an optical section during NC dumping, showing an increase in intensity and change in distribution. Scale bar = 20 μm. **B**. Swarm plot of the coefficient of variation of Sqh intensity along the cell perimeter in NCs prior to the onset of NC dumping (pre-NC dumping), and during Phases I and II of NC dumping, showing a statistically significant difference in Sqh distribution (p-value < 0.05) ($N = 4$ cells; 534 measurements). **C**. Swarm plot as in **B**. showing the coefficient of variation of Resille (a membrane marker) intensity at the cell perimeter in NCs, showing no statistically significant changes in its distribution prior to NC dumping, or between Phases I and II (p-value > 0.05; $N = 5$ cells; 504 measurements). Horizontal lines and error bars represent means and standard error, respectively; colored spots represent the mean of each NC.
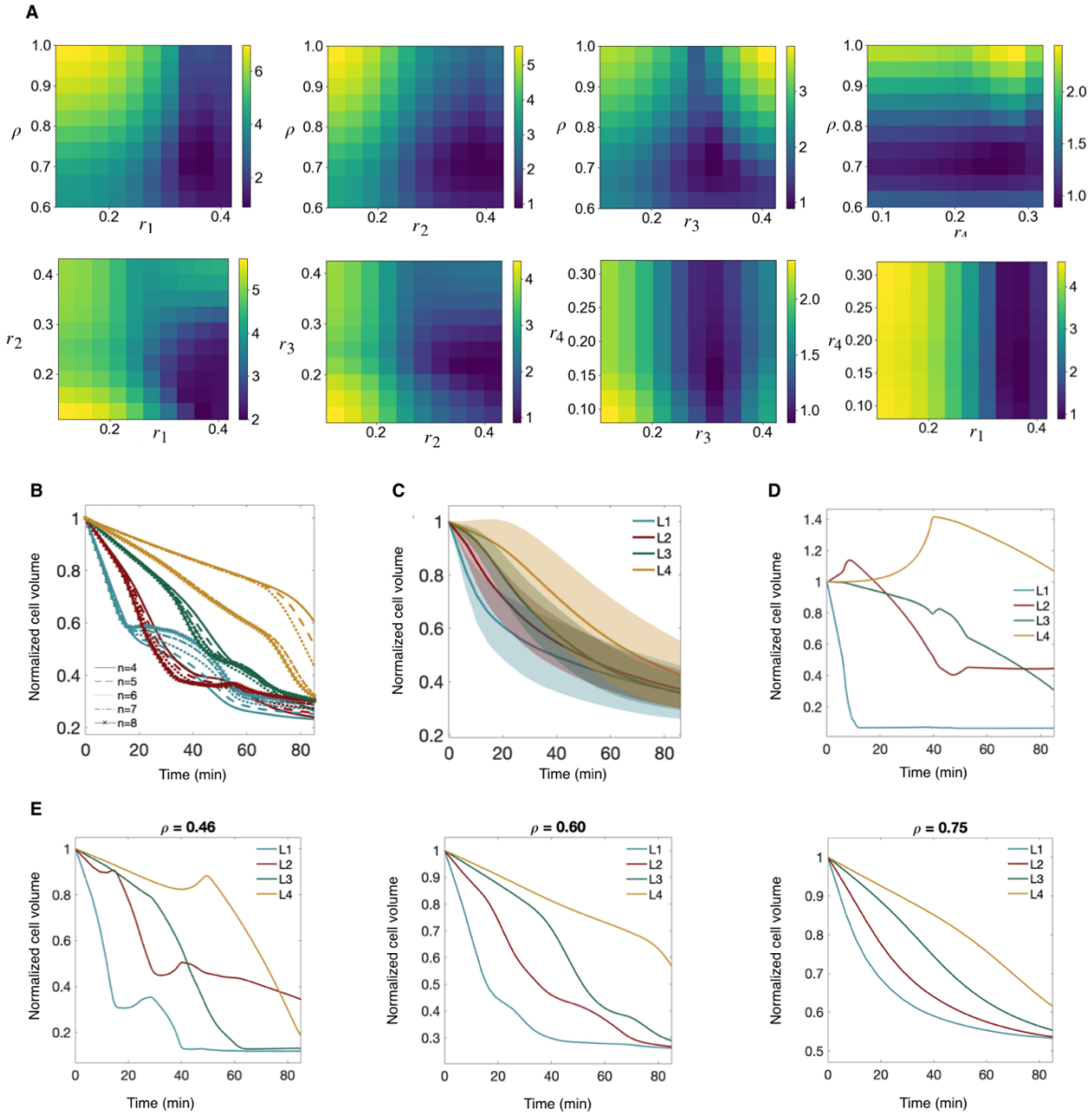
Fig. S4. Grid search through parameter space and effects of input parameters of the model. A. Two-dimensional slices of the simulation error as defined in *Methods* measured on the 5-dimensional grid space spanned by the sampled parameter ranges $(r_1, r_2, r_3, r_4, \rho)$. For a given pair of parameters, the remaining parameters are at their best-fit values. Color bar refers to simulation error ($\sigma = 0.1$; see *Methods*). **B**. Normalized NC volume (V/V_o) from simulations for varying values of n, the exponent in the correction term to the Young-Laplace law, showing that intercellular transport hierarchy and qualitative behaviors are maintained for the values of n tested. **C**. Results from simulations averaged over 5,000 trials, where surface tension of each cell is sampled from a normal distribution; envelope reflects half a standard deviation of the fluctuations. As seen in the envelope for L4, in several of these simulations the L4 cell increases in size due to backflow from its downstream L3 cell - a feature of NC dumping that has been reported in previous

17

studies (20). **D**. Results from simulations showing layer-wise averaged cell volumes over time, in which all NCs and ring canal radii are equal for all cells, showing qualitative differences in the intercellular pattern and time scale of transport. **E**. Results from simulations for three values of ρ and all ring canal sizes at their best-fit values. Smaller values of ρ show transient increases in layer size indicative of backflow, while larger values result in less backflow and smoother curves.
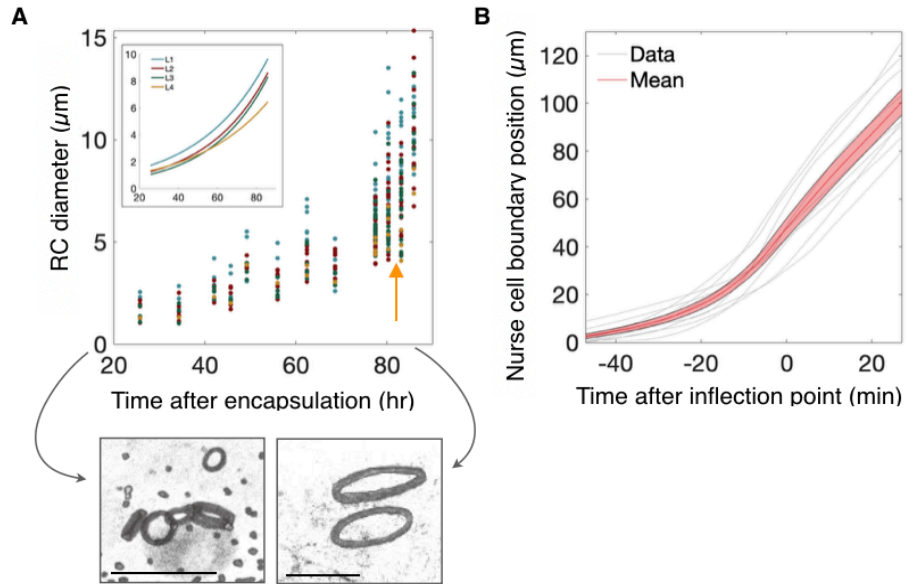
Fig. S5. Effective ring canal size increases in the latter stages of oogenesis. A. Increase in ring canal diameter during oogenesis, with rapid growth occurring in the latter stages of oogenesis (arrow). Inset shows exponential fits to ring canal diameters of the form $d(t) = d_o e^{t/\tau}$ where $d_o = 0.78, 0.43, 0.36, 0.64 \mu m$, $\tau = 34.8, 31.2, 29.1, 38$ hours; $R^2 = 0.93, 0.88, 0.85, 0.83$ for L1-L4, respectively. Layers are colored as in Figure 2. Arrows point to 3D-rendered confocal images of ring canals at ~20 and ~80 hours after encapsulation of the germline cyst (i.e. oogenesis Stage 1). Scale bar = 10 μm. **B**. Measurements of the position of the most-posterior edge of the NC cluster over time, where $t = 0$ is fastest rate of change in position of said edge (envelope shows standard error; $N = 9$ egg chambers).
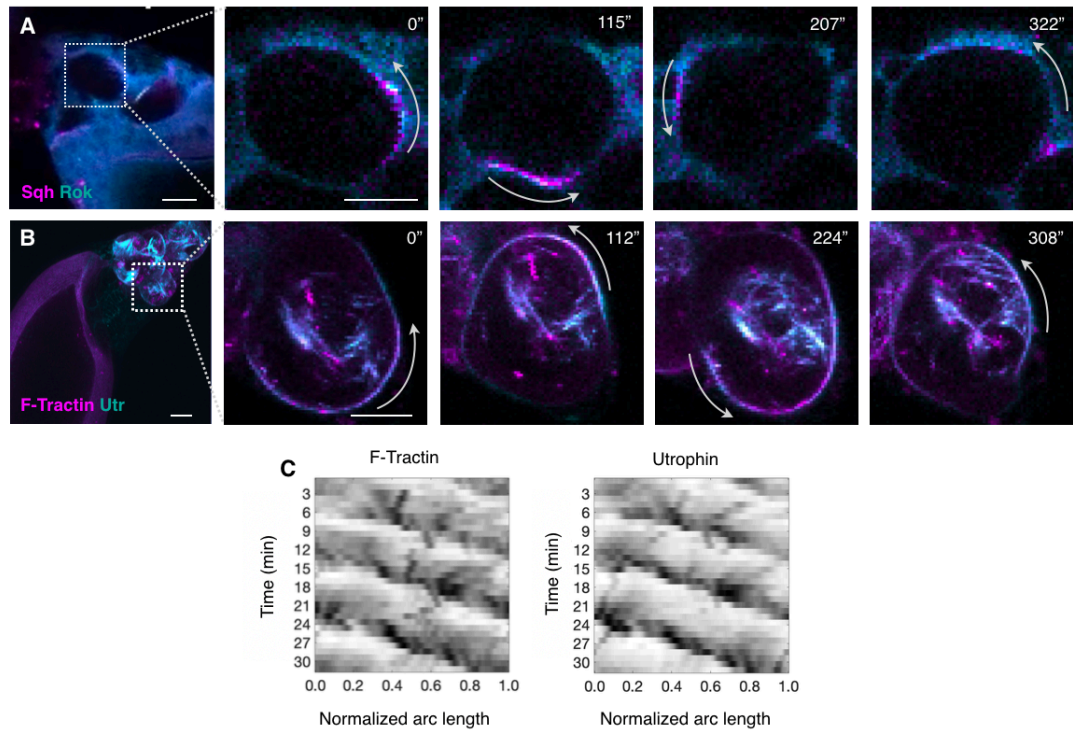
Fig. S6. Rho-regulated actomyosin wave dynamics during NC dumping. A. Egg chamber expressing *sqh::mCh* (magenta) and *ubi>GFP::rok* (cyan). Rok, upstream of Sqh, exhibits similar wave-like dynamics as seen in blowup as bands rotating along the NC cortex (arrows). **B**. Egg chamber expressing *F-tractin::TdTom* (magenta) and *Utr::GFP* (cyan); blowup shows both actin-binding proteins exhibiting wave-like dynamics, with bands rotating along the cell cortex (arrow). Scale bars in **A** and **B** = 20 μm. **C**. Kymographs of F-tractin and Utrophin wave dynamics during actomyosin-mediated phase of NC dumping; black indicates highest intensity.
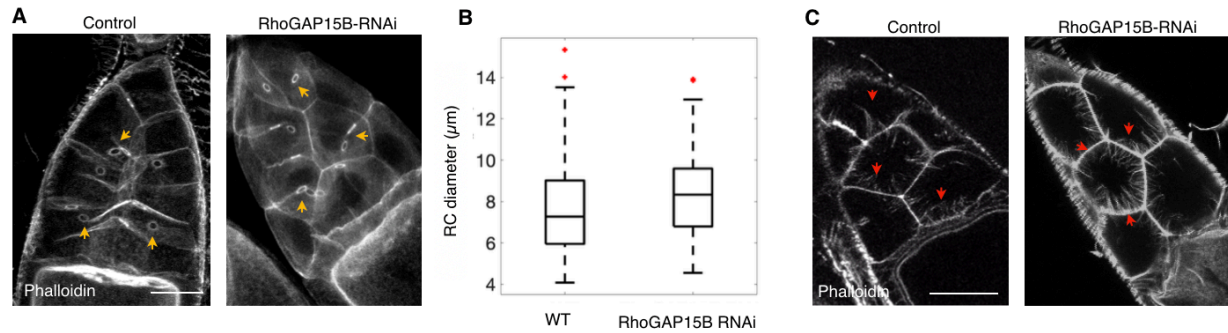
Fig. S7. Ring canals and actin cables in WT and RhoGAP15B-depleted egg chambers. A. 3D images of a control egg chamber (left) and an egg chamber with a RhoGAP15B-depleted germline cyst (right) stained with Phalloidin to show comparable ring canal structure to WT (arrows). **B**. Box plot of ring canal diameters (μm) in WT and in RhoGAP15B germline knockdowns ($N = 162$ ring canals for WT; 142 for RhoGAP15B-RNAi at oogenesis stage 10 and 11; red pluses mark data points > 1.5xIQR from median). **C**. Optical section of a control egg chamber (left) and an egg chamber with a RhoGAP15B-depleted germline (right) stained with Phalloidin; arrows point to actin cables that extend from the cell cortex to tether NC nuclei during NC dumping. Scale bar in **A** and **C** $= 40$ μm.
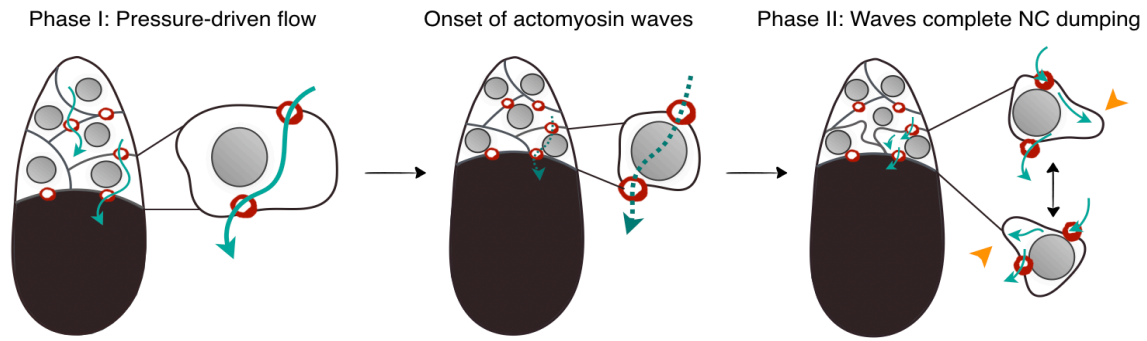
Fig. S8. Physical and biochemical mechanisms cooperate to enable NC dumping. Schematic of the proposed model for the contribution of pressure-driven flow with baseline cortical tension and actomyosin-dependent flows to directional and complete NC dumping. Arrows show direction of intercellular flow; dashed arrow indicates interrupted flow; arrowheads point to actomyosin-mediated cell deformations that permit continued intercellular flow in shrunken NCs.

Tables S1 to S3

Table S1. Fly stocks used in this study, their source, and figures in which they appeared.

Transgene name	Source[*]	Relevant to:
ubi>Pav::mCh	gift from Dr. Emmanuel Derivery	Figure 1
PCNA::GFP	gift from Dr. Eric Wieschaus	Figure 1, Figure S2
Resille::GFP/+; PCNA::GFP/pav::mCh	Lab stocks	Figure 1
Ecad:GFP	Lab stocks	Figure 1, Figure S1
sqh::mCh; *ubi>GFP::rok*	Lab stocks	Figure S6
UASp-F-tractin::TdTom	BDSC (58989)	Figure S6
Pdi::GFP	BDSC (6839)	Figure S7
TJ-Gal4; *H2A::GFP, gap43::mCh*	Lab stocks	Figure 4
mat67, sqh::mCh; GFP::Clip170/Tm3	Lab stocks	Figure 1, Figure 3, Figure S2
w; sqh::GFP, gap43::mCh	Lab stocks	Figure S3
Resille::GFP	Lab stocks	Figure S3
mat67, Utr::GFP	Lab stocks	Figure S6
sqh[1] *FRT101/FM7; sqh::GFP/CyO*	Lab stocks	Figure 2[†]
ovoD FRT101/C(1)DX; hsFlp[38]	BDSC (1813)	Figure 2[†]
y[1] v[1]; P{TRiP.HMJ02093}attP40/CyO	BDSC (42527)	Figure 3, Figure 4, Figure S7[‡]

[*] BDSC: Bloomington *Drosophila* Stock Center; VDRC: Vienna *Drosophila* Resource Center.

[†]*sqh[1]* germline generated using the FLP-DFS technique by crossing *sqh[1] FRT/FM7; sqhTS::GFP/CyO* females to *ovoD FRT; hsFlp* males and heat shocking *sqh[1] FRT/ovo[D] FRT; CyO/hsFlp* embryos for 2 hours at 37°C for 3 - 4 days *(22)*. A control lacking heat shock verified the presence of the *ovo[D]* allele.

[‡]RhoGAP15B-RNAi knockdown flies were generated by crossing virgins of the shRNA line #42527 to mat67 drivers caring fluorescent markers (*mat67, sqh::mCh; GFP::Clip170/Tm3*). F1 females with *mat67, sqh::mCh*/P{TRiP.HMJ02093}attP40*; GFP::Clip170/+* were used for experiments.

Table S2 | Measurement types and sample sizes used to generate the figures.

Figure	Measurements	N	Number of egg chambers
1D	Deformation and projected area	4 cells	2
1E	Myosin COV; points are measurements at different timepoints	534 measurements from 4 cells	2
2C	Cell size over time	41 cells total	8
2I	Cell size over time	44 cells total	5
3F	Wave onset time	63 cells total	10
3I	Cell size over time	18 cells total	4
4E	Intercellular flow behaviors	WT: 6 events spanning 30 minutes; RhoGAP15B: 29 events spanning 54 minutes	2 (WT), 7 (RhoGAP15B)
4F	Intracellular flow behaviors	WT: 28 events spanning 239 minutes; RhoGAP15B: 82 events spanning 338 minutes	2 (WT), 7 (RhoGAP15B)
S1A	Length of NC cluster and oocyte	4	4
S1D	Cell sizes from FIJI and Imaris	39 measurements from 9 cells	4
S2B	Wave onset time	63 cells total	10
S2E	Size over time	30 cells total	8
S3B	COV of Sqh	534 measurements from 4 cells	2
S3C	COV of Resille	504 measurements from 5 cells	2
S5A	Ring canal diameter	370 ring canals	26
S5B	Nurse cell boundary position	9 egg chambers	9
S7B	Ring canal radii at stages 10-11	WT: 162 ring canals; RhoGAP15B: 144 ring canals	11 (WT), 10 (RhoGAP15B)

Table S3 | Summary of initial conditions and parameters used in the mathematical model.

Fixed			Optimized		
Layer	**# of cells**	**Initial volume***	**Parameter**	**Parameter range†**	**Best fit‡**
Oocyte	1	100	ρ	$[0.22, 1]$	0.60
1	4	9.00	$\hat{G}_1$	$[1.5 \times 10^{-4}, 3.4 \times 10^{-2}]$	1.7×10^{-2}
2	6	6.61	$\hat{G}_2$	$[1.5 \times 10^{-4}, 3.4 \times 10^{-2}]$	2.3×10^{-2}
3	4	5.07	$\hat{G}_3$	$[2.9 \times 10^{-4}, 2.6 \times 10^{-2}]$	8.1×10^{-3}
4	1	4.03	$\hat{G}_4$	$[1.0 \times 10^{-4}, 8.1 \times 10^{-3}]$	4.6×10^{-3}

*Given in units of $\ell_0^3 = 8 \times 10^3 \mu m^3$.

† The scanned range of the dimensionless hydraulic conductances $\hat{G}_d$ corresponds to a range of effective ring canal radii $r_d := \ell_0 \hat{G}_d^{1/4}$ within ±60% of the experimentally measured average ring canal size for each layer.

‡Best fit parameters minimize the error as defined in section 'Simulations and Optimization' above.

Movies S1 to S10

Movie S1. Part I: Maximum intensity projection (MIP) of an egg chamber expressing *Ecad::GFP*. The shrinking NC cluster moves anteriorly (top) as NCs transport their cytoplasm into the growing posterior oocyte (bottom). Movie length: 4.5 hours; 64-second intervals. Scale bar 50 μm, 1300x real time. Part II: Reflection-mode microscopy of an egg chamber showing intercellular movement of NC cytoplasm (cyan) through ring canals (arrows) towards the oocyte (positioned left) during NC dumping. Movie length: 39 seconds, with 0.5-second intervals. Scale bar 20 μm, 10x real time.

Movie S2. MIP generated from 4D live imaging of an egg chamber expressing *sqh::mCh* (red) to label myosin and *PCNA::GFP* (cyan) a to mark the cells' nuclei. Onset of NC dumping and transport of most of NC volume occurs as NC shrink uniformly without undergoing cell shape deforming contractions. Nonuniform cell contractions commence at 1 hour, 29 minutes (arrow), when NC volume has decreased by 75%. Movie length: 2 hours 20 minutes; 20-second time points. Scale bar 50 μm, 400x real time.

Movie S3. Heat map of an average intensity projection generated from 4D live imaging of an egg chamber expressing *sqh::GFP*. White line indicates position of NC-oocyte boundary at the onset of NC dumping. As NC unfolds, NC actomyosin cortical pattern changes from a uniform to a non-uniform and dynamic pattern, coincident with onset of contractile NC shape deformations. Movie length: 54 minutes; 20-second time points. Scale bar 50 μm, 480x real time.

Movie S4. Animation of NC dumping on the 16-cell network based on the flow network model, starting with experimentally determined sizes and showing the evolution of cell radii according to the simulation best fit. Ring canals are red when flow proceeds towards the oocyte; blue canals indicate backwards flow. Animation was generated using matplotlib in Python and is approximately 1000x real time.

Movie S5. MIP generated from 4D live imaging of a *sqh^1* egg chamber stained with CellMask (magenta). Despite a reduction of ~90% of Sqh mRNA and protein levels, the first and second NC layers (cyan and red arrows, respectively) nonetheless empty their contents into the oocyte. Transport is however incomplete, leading to a dumpless phenotype. Movie length: 2.5 hours; 30-second time points. Scale bar 50 μm, 720x real time.

Movie S6. MIPs from 4D live imaging of egg chambers expressing *sqh::mCh* (red) and *Clip170::GFP* (cyan) to mark cells' myosin and cytoplasm, respectively, highlighting the diversity of actomyosin wave-like behaviors. Left movie shows an example of myosin rings travelling between the cell's poles (white arrow); right movie shows examples of a colliding myosin wave fronts (yellow arrow) and a rotating cortical band (gray arrow). Movie lengths: 83 minutes with 28-second time points (left); 51 minutes with 17-second time points (right). Scale bar 50 μm; left movie 670x real time, right movie 410x real time.

Movie S7. MIP generated from 4D live imaging of an egg chamber expressing *utr::GFP* (cyan) and *F-tractin::TdTom* (magenta), showing similar wave-like dynamics as myosin. Movie length: 2 hours, 53 minutes; 28-second time points. Scale bar 50 μm, 670x real time.

Movie S8. MIP generated from 4D live imaging of egg chamber with a RhoGAP15B depleted germline, expressing *Clip170::GFP* (cyan, left) and *sqh::mCh* (red, right) to mark cells' myosin and cytoplasm. RhoGAP15B knockdowns exhibit disrupted actomyosin dynamics in Phase II of NC dumping and do not complete transport, resulting in a remnant NC cluster and a dumpless phenotype. Movie length: 113 minutes; 35-second time points. Scale bars 50 μm, 840x real time.

Movie S9. Left: Live imaging of one slice of an egg chamber, obtained using reflection-mode microscopy to capture cytoplasmic movement (cyan) and stained with CellMask (white) to show cell membranes. As dumping unfolds, cells deform dynamically. Inset: oocyte-NC cluster boundary (yellow line) at NC dumping onset. Movie length: 24 minutes; 10-second time points. Scale bar 50 μm. Right: Blow-up of one slice of a single NC; contractile shape deformations enable continuous cytoplasmic flow past nuclei once nurse cell volume has become comparable to the nuclear volume, thus enabling complete dumping. Movie length: 24 minutes; 10-second time points. Scale bar 20 μm. Both movies are 250x real time.

Movie S10. Part I: Live imaging movie showing a single slice of a RhoGAP15B depleted egg chamber during NC dumping, captured using reflection mode microscopy to highlight the NCs' cytoplasm (cyan). Intracellular flow in RhoGAP15B knockdowns lacks the persistent radial motions around NC nuclei that are observed in WT, instead exhibiting short-lived and erratic protrusions. Part II: reflection-mode microscopy movie of the boxed region highlights rapid reversal of flow direction from anterior-to-posterior (A-to-P, i.e. towards the oocyte) to P-to-A flow through the ring canals (yellow arrow under the ring canal indicates direction). Movie lengths: 170 seconds; 4.6-second intervals, and 298 seconds; 1.4-second intervals. Scale bars 20 μm, 90x real time and 30x real time.

References

1. J. Schindelin *et al.* Fiji: an open-source platform for biological-image analysis. *Nat. Methods* **9**, 676-682 (2012).

2. Bitplane Inc. Imaris Version 9.3.0, imarisxt. Zurich, Switzerland

3. MATLAB, 2018. *9.5.0.1033004 (R2018b)*, Natick, Massachusetts: The MathWorks Inc.

4. Y. Shimada, M. K. R. Mahala Burn, L. Niwa, L. Cooley. Reversible response of protein localization and microtubule organization to nutrient stress during *Drosophila* early oogenesis. *Dev Biol.* **355**, 250-262 (2011).

5. H. Lin H, A.C. Spradling, Germline stem cell division and egg chamber development in transplanted *Drosophila* germaria. *Dev. Biol.* **159**, 140-152 (1993).

6. K. Doubrovinski, M. Swan, O. Polyakov, E. F. Wieschaus. Measurement of cortical elasticity in *Drosophila melanogaster* embryos using ferrofluids. *Proc. Natl. Acad. Sci. U.S.A.* **114**, 1051-1056 (2017).

7. D.R. Merrit, F. Weinhaus, The pressure curve for a rubber balloon. *Am. J. Phys.* **46**, 976-977 (1978).

8. A.R. Bausch, K. Kroy. A bottom-up approach to cell mechanics. *Nat. Phys.* **2**, 231-238 (2006).

9. H.M. James, E. Guth. Theory of the Elastic Properties of Rubber. *J. Chem. Phys.* **11**, 455 (1943).

10. E. Verron, R.E. Khayat, A. Derdouri, B Peseux, Dynamic inflation of hyperelastic spherical membranes. *J. Rheol.* **43**, 1083-1097 (1999).

11. R. Vargas-Pinto, H. Gong, A. Vahabikashi, M. Johnson. The effect of the endothelial cell cortex on atomic force microscopy measurements. *Biophys. J.* **105**, 300-309 (2013).

12. T. Lecuit, P. Lenne. Cell surface mechanics and the control of cell shape, tissue patterns and morphogenesis. *Nat. Rev. Mol. Cell Biol.* **8**, 633-644 (2007).

13. D.J. Acherson, *Elementary Fluid Dynamics* (Clarendon Press, Oxford, 1990).

14. A. Diz-Muñoz, D. A. Fletcher, O. D. Weiner. Use the force: Membrane tension as an organizer of cell shape and motility. *Trends Cell Biol.* **23**, 47-53 (2013).

15. C.E. Morris, U. Homann. Cell surface area regulation and membrane tension. *J. Membr. Biol.* **179**, 79-102 (2001).

16. J. Chlasta *et al.* Variations in basement membrane mechanics are linked to epithelial morphogenesis. *Development* **144**, 4350-4362 (2017).

17. J.J. Thottacherry *et al.* Mechanochemical feedback control of dynamin independent endocytosis modulates membrane tension in adherent cells. *Nat. Commun.* **9**, 4217 (2018).

18. N.P. Gonzalez, J. Tao, N. D. Rochman, D. Vig, E. Chiu, D. Wirtz, S.X. Sun. Cell tension and mechanical regulation of cell volume. *Mol. Biol. Cell.* **29**, 2591-2600 (2018).

19. J. Imran Alsous, P. Villoutreix, A.M. Berezhkovskii, S.Y. Shvartsman, Collective growth in a small cell network. *Curr. Biol.* **27**, 2670-2676 (2017).

20. H.O. Gutzeit, The role of microfilaments in cytoplasmic streaming in *Drosophila* follicles. *J. Cell Sci.* **80**, 159-169 (1986).